# Ultrasound-Driven Programmable Artificial Muscles

Zhan Shi[1]†, Zhiyuan Zhang[1]†, Justus Schnermann[2], Stephan C. F. Neuhauss[3], Nitesh Nama[4], Raphael Wittkowski[2,5], Daniel Ahmed[1]*

**Affiliations:**
[1]Acoustic Robotics Systems Laboratory, Institute of Robotics and Intelligent Systems, Department of Mechanical and Process Engineering, ETH Zürich, 8803 Zürich, Switzerland.
[2]Institute of Theoretical Physics, Center for Soft Nanoscience, University of Münster, 48149 Münster, Germany.
[3]Department of Molecular Life Sciences, University of Zürich, 8057 Zürich, Switzerland.
[4]Department of Mechanical & Materials Engineering, University of Nebraska-Lincoln, 68588 Lincoln, Nebraska, USA.
[5]Department of Physics, RWTH Aachen University, DWI-Leibniz Institute for Interactive Materials, 52074 Aachen, Germany.

*Corresponding author. Email: dahmed@ethz.ch

†These authors contributed equally to this work.

**Abstract**
Muscular systems[1,2], the fundamental components that enable mobility in the majority of animals within the Animalia kingdom, have sparked innovations in various technological and medical fields[3,4]. Despite their promises, artificial muscles encounter critical bottlenecks in dynamic programmability, scalability, and responsiveness attributed to the complexities of their actuation mechanisms and the specific requirements of the materials used. Here, we introduce a design paradigm for artificial muscles, utilizing >10,000 microbubbles with targeted ultrasound activation. These microbubbles are engineered with precise dimensions that correspond to distinct resonance frequencies. When stimulated by a sweeping-frequency ultrasound, microbubble arrays in the artificial muscle undergo selective oscillations and generate distributed point thrusts, enabling the muscle to achieve programmable deformation with remarkable attributes: a high compactness of around 3,000 microbubbles/mm², a low weight of 0.047 mg/mm$^2$, the ability to generate a substantial force intensity of ~1.21 μN/mm$^2$, and fast response (sub-100 ms during gripping). Moreover, they offer good scalability (from micro- to centimeter scale), exceptional compliance, and many degrees of freedom. We support our approach with a theoretical model and demonstrate applications spanning flexible organism manipulation (e.g., handling zebrafish larvae), conformable robotic skins for adding mobility to static objects, multimodal shape-shifting surfaces, and biomimetic stingraybots for propulsion. The customizable, scalable design of our artificial muscles could offer both immediate and long-term impact on soft robotics, wearable technology, haptics, and the development of avant-garde biomedical devices like soft surgical tools.

**Main**

Flexible, compact, and adaptive artificial muscles, are set to be transformative across multiple fields, including soft robotics[5,6], wearables for human-machine interactions and healthcare, like prosthetics[7,8], orthotics[9,10], and embodied sensing[11,12], and assistance in sophisticated manufacturing through dexterous manipulation[13,14]. In biomedicine, they could revolutionize soft surgical tools[15,16], implantable electrodes[17,18], and artificial organs like the heart[19,20]. Despite their potential, current artificial muscles like tendon-based[21,22] and pneumatic types[23,24] encounter substantial challenges in wireless control, integration, and miniaturization due to dependencies on tethering, complex operational mechanisms, and large input requirements. While external stimuli such as chemicals[25,26], light[27-30], temperature[31-33], electric fields[34–36], and magnetic fields[37–40] have been deployed for wireless actuation, they face challenges in biocompatibility, spatial resolution, and dynamic programmability. Chemical methods often require fuels that could be toxic[41], light-based systems suffer from limited tissue penetration and potential thermal damage[42], and magnetic systems necessitate bulky hardware while risking Joule heating[43]. In contrast, acoustic actuation emerges as a promising biocompatible alternative. It offers wireless control, millisecond-scale responsiveness, and deep tissue penetration without invasive hardware —making it uniquely suited for in vivo and broader biomedical applications[44–52].

Central to this approach are resonant microbubbles, which concentrate acoustic energy and enable weak ultrasound sources to generate amplified responses. While prior ultrasound-actuated microrobots and actuators have employed single or sparse microbubbles embedded in polymers to achieve basic propulsion[53-56], their functionality remained limited. Directional steering has been demonstrated through strategies such as tuning microbubble sizes[57], applying magnetic navigation[58-60], or hybrid methods that combine magnetic fields with asymmetric appendages in encapsulated shells[61]. An actuator composed of a microbubble attached to a flexible beam was developed to analyze the kinematic behavior of some simple microstructures through the excitation of different pairs of bubble actuator modules[62]. Another study utilized arrays of microbubbles integrated onto centimeter-scale rigid substrates to induce bi-rotational motion[63], demonstrating potential applications in endoscope design[64]. However, these systems lack the programmability, scalability, and dynamic adaptability required to emulate natural muscle behavior. Critically, to the best of our knowledge, no prior work has achieved ultrasound-actuated soft artificial muscles, marking a significant gap in biologically inspired actuation technologies.

Why did ultrasound-based artificial muscles remain undeveloped? Soft materials typically exhibit low acoustic contrast factors compared to water, leading to inadequate force generation for efficient functionality when activated by ultrasound. This inadequacy becomes more pronounced at larger scales, which requires lower frequencies and thus lower damping to match their increased dimensions. This predicament is exacerbated by a lack of understanding of the interactions between sound and complex soft materials, impeding the progress of effective sound-driven muscle systems. However, we found that integrating ultrasound-activated microbubble arrays into soft artificial muscles presents a clever approach that could potentially address these limitations.

Here, we introduce an artificial muscle built on acoustically activated microbubble arrays. This synthetic muscle comprises a thin, transparent, and flexible membrane that houses over 10,000 microcavities arranged in arrays, designed to confine microbubbles of various sizes. When these microbubbles are acoustically stimulated, they generate thrust, causing the membrane to deform. Tailored activation of differently sized microbubble arrays through programmable sweeping-

frequency ultrasound excitation results in localized point forces, allowing dynamic multi-modal deformation of the artificial muscle. The tunable nature and scalability of these microbubble arrays herald a new era of possibilities, positioning these acoustic artificial muscles at the forefront of innovation in robotics, wearable technology, prosthetic development, and soft surgical devices.

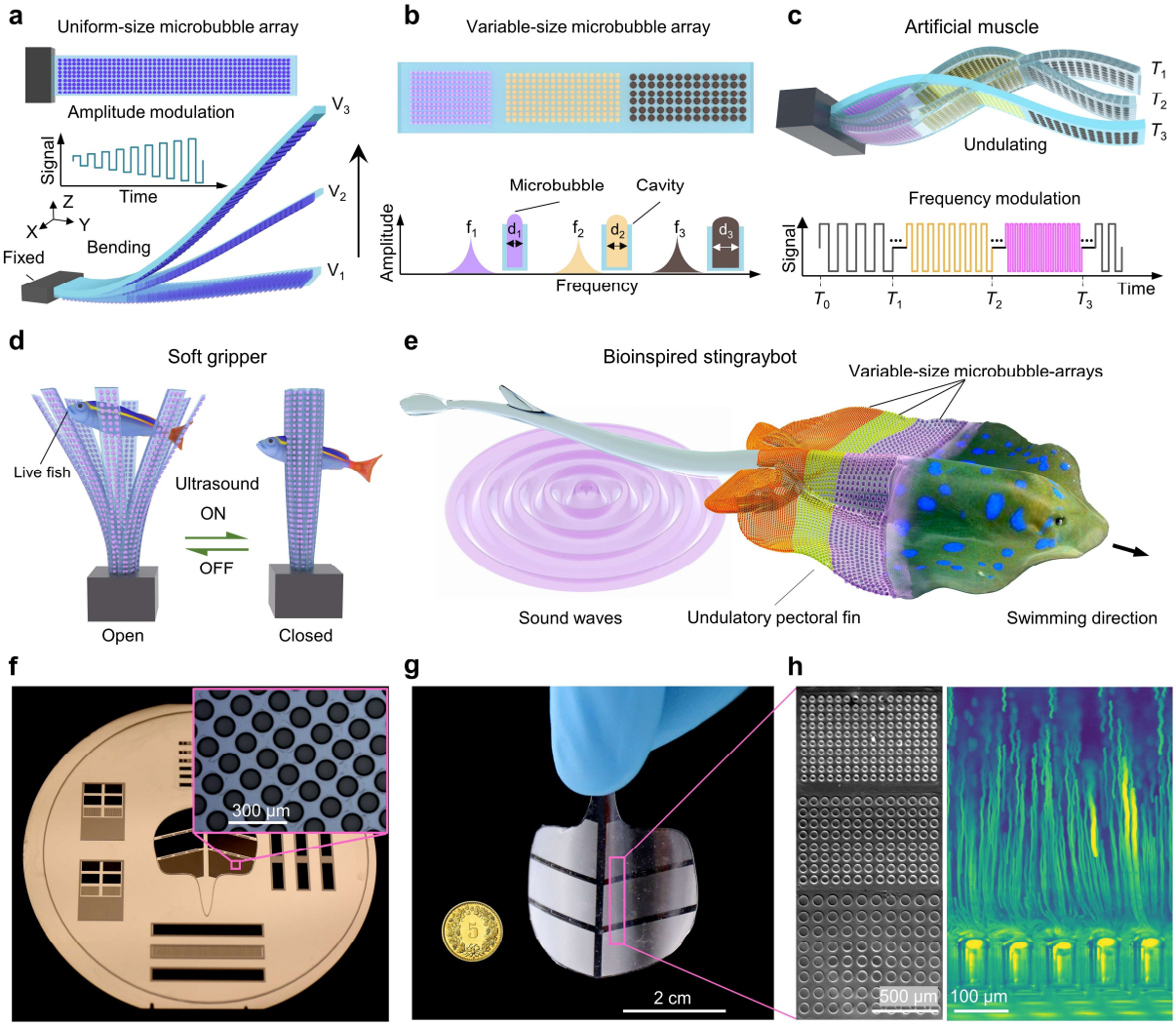


**Fig. 1 | Ultrasound-actuated microbubble-array artificial muscles. a**, A uniform-size microbubble-array artificial muscle consists of thousands of microbubbles on its bottom surface. Under continuous ultrasound excitation, the artificial muscle bends upwards with different excitation voltages, labeled as $V_1$, $V_2$, and $V_3$. The inset shows the input ultrasound signal with modulated amplitude versus time. **b**, A variable-size microbubble-array artificial muscle consists of three microbubble arrays with different microbubble diameters featuring different natural frequencies represented by distinct colors. **c**, Under sweeping-frequency ultrasound excitation, the artificial muscle exhibits multi-mode deformation in the time domain, shown at time points $T_1$, $T_2$, and $T_3$. **d**, Schematic of a soft gripper constructed with an array of artificial muscles patterned with uniform-size microbubble arrays. Upon ultrasound excitation, these muscles close simultaneously in milliseconds. **e**, Schematic of a bioinspired stingraybot incorporates variable-size microbubble array artificial muscles. Under sweeping-frequency ultrasound excitation, the stingraybot enacts

undulating propulsion. **f**, A silicon wafer with micropillar arrays serves as the negative mold of microbubble cavities in standard soft-lithography fabrication. Inset shows the micropillar array. **g,** A prototype of the stingraybot. Inset shows a 5-cent Swiss franc coin. **h**, Left: Trapped microbubbles on the stingraybot. Right: Upward microstreaming jetting generated from a microbubble array oscillating under ultrasound excitation demonstrated by 6 μm diameter tracer microparticles.

## Results

### Design and fabrication of microbubble-array artificial muscles

In the initial design of the ultrasound-driven artificial muscle (**Fig. 1a**), we incorporated uniform-size microcavities on the muscle's bottom surface. When the muscle was submerged in an acoustic chamber filled with water, it resulted in the simultaneous trapping of tens of thousands of gas-filled microbubbles within these cavities, a phenomenon driven by surface tension[65]. To test the muscle's actuation, we anchored one end and left the other free, forming a cantilever configuration. Subsequently, we activated a piezoelectric transducer to generate ultrasound. The incident sound waves propagated through the liquid, triggering oscillations in the microbubbles. Since all microbubbles in the muscle were of identical dimensions, they were simultaneously excited. This harmonic bubble oscillation generated collective acoustic streaming and radiation forces, applying a uniform opposing force to the muscle's bottom surface and resulting in upward flexion. By modulating the ultrasound excitation voltage, we controlled the deformation amplitude of the artificial muscle.

We then designed an artificial muscle featuring microbubble arrays of varying bubble sizes, illustrated in **Fig. 1b**. Since microbubbles of different sizes exhibit distinct resonance frequencies[66], they can be independently activated to produce localized opposing forces and selective muscle deformation. By applying a sweeping-frequency ultrasound signal that encompasses the natural frequencies of all microbubbles, we sequentially activated distinct arrays along the muscle's longitudinal axis. This orchestrated activation generated complex undulatory motion across multiple excitation cycles (**Fig. 1c**). Thus, in implementing this arrangement of microbubbles of varied sizes and their frequency-selective excitation through ultrasound modulation, we have unlocked a capability to control multi-modal deformations. The versatility of these artificial muscles facilitates a wide array of applications. For example, we implemented these artificial muscles in the development of a soft gripper, crafted to delicately handle live fish (**Fig. 1d**), and in the design of a soft swimmer, inspired by the form and function of stingrays (**Fig. 1e**), among other functional systems.

Prototypes of these artificial muscles were fabricated using a high-resolution mold replica method. First, micropillar arrays were patterned on a silicon wafer using soft lithography to serve as negative molds for cylindrical microcavities (**Fig. 1f**). All pillars were designed of identical heights and spacings, corresponding to dimensions of desired microbubbles (**Supplementary Fig. 1**). A thin layer of polydimethylsiloxane (PDMS) was then spin-coated onto the wafer, yielding uniform thicknesses ranging from 80 μm to 250 μm (**Extended Data Fig. 1**). After curing, these artificial muscles including the artificial stingray (**Fig. 1g)** were demolded, sectioned, and prepared for testing. Full fabrication details are provided in the Materials and Methods section. **Figure 1h** demonstrates microbubbles trapped on the "stringraybot" and the upward microstreaming jets produced during ultrasound excitation.

**Characterization of microbubble arrays**

To further our understanding and control of microbubble arrays in artificial muscles, we examined the interaction between microbubble arrays and ultrasound signals. Our experimental setup included a transducer bonded onto a glass slide, positioned adjacent to a miniaturized water-filled acoustic chamber (10 mm × 10 mm × 5 mm), and an artificial muscle was suspended in the center of the chamber with one end clamped to the sidewall and the other end left free (**Supplementary Fig. 2**). The entire assembly was mounted on an inverted microscope. Using a high-speed camera, we observed the transient dynamics of the microbubbles while applying acoustic fields with excitation frequencies of 10−100 kHz and voltage amplitudes of 10−60 $V_{PP}$ in square waveforms, which effectively drove the artificial muscle, enabling maximum deformation and outperforming other tested waveforms, such as sinusoidal and triangular waveforms under equivalent excitation conditions (**Supplementary Fig. 3**). Further details on the acoustic setup are provided in the **Materials and Methods** section.

We began by identifying the resonance frequency of microbubbles confined within cavities with different diameters (40−140 μm, in 10 μm increments) and depths (50 μm, 150 μm, and 175 μm) while maintaining a constant excitation voltage of 15 $V_{PP}$. Resonance frequencies were identified by locating peak oscillation amplitudes during frequency sweeps (**Extended Data Fig. 2a)**. As shown in **Extended Data Fig. 2b**, resonance frequencies decreased from 95.5 kHz to 8.9 kHz with increasing microbubble diameter, consistent with the inverse scaling relationship between the natural frequency and the bubble diameter[67]. Microbubbles of different depths 50 μm (purple line), 150 μm (green line), and 175 μm (blue line) exhibited a reduction in the resonance frequency, indicating that the bubble depth also affects bubble oscillation. The distinct resonance profiles of microbubbles across sizes enable selective ultrasound excitation, forming the basis for programmable microbubble arrays.

Building on the resonance frequency characterization, we then evaluated the microstreaming jets generated by ultrasound-driven microbubbles embedded in the muscle, using 6 μm tracer particles in water and particle image velocimetry (PIV) analysis. Three uniform-size microbubble arrays, each comprising a 4×4 grid of microbubbles with diameters of 40 μm, 60 μm, and 80 μm (150 μm in depth), were individually tested in separate miniaturized artificial muscles (500 μm × 500 μm × 200 μm) (**Extended Data Fig. 3a** and **Supplementary Video 1**). When activated at their respective resonance frequencies 76.3 kHz, 57.4 kHz, and 27.6 kHz, we measured the microstreaming velocity 80 μm away from the bubble interface and observed a quadratic relationship between the average velocity and excitation voltage (**Extended Data Fig. 3b**). The streaming velocity near the bubble reached 2.5 mm/s at 60 $V_{PP}$. This voltage-dependent microstreaming directly correlates with the reverse thrust generated by the microbubble array, demonstrating that thrust magnitude can be dynamically tuned by adjusting the ultrasound excitation.

We further investigated the selective actuation of a variable-size microbubble array with bubble diameters of 40 μm, 60 μm, and 80 μm, each 150 μm in depth, integrated within a single artificial muscle (500 μm × 500 μm × 200 μm), as demonstrated in **Extended Data Fig. 4** and **Supplementary Video 2**. The PIV analysis reveals that the microstreaming developed by the 80 μm bubbles generated an average velocity of 0.23 mm/s at 27.6 kHz, which was markedly stronger compared to the velocities produced by the other two microbubble arrays at the same voltage (15 $V_{PP}$). Although the microstreaming velocity around the other bubble arrays was not negligible, it

was markedly lower, at less than 0.05 mm/s. Applying a sweeping frequency (10–90 kHz) over 4 seconds at 30 $V_{PP}$ enabled wave propagation across the artificial muscle (**Supplementary Video 3**). While our experiments demonstrated frequency-dependent selectivity in microbubble activation, we observed cross-excitation between differently sized arrays, likely arising from resonance coupling effects between neighboring microbubbles. However, the effect of cross-excitation is reduced when using a sweeping frequency due to the temporal separation of the excitation. During the sweep, each resonance frequency briefly activates its corresponding microbubble array (lasting milliseconds), while streaming from cross-excited microbubbles remains weaker and develops more slowly. By optimizing the sweep rate (e.g., transitioning speed between frequencies), the time window for cross-excitation effects is narrowed. This temporal control suppresses unintended microstreaming contributions, ensuring the artificial muscle's motion closely follows the programmed actuation sequence.

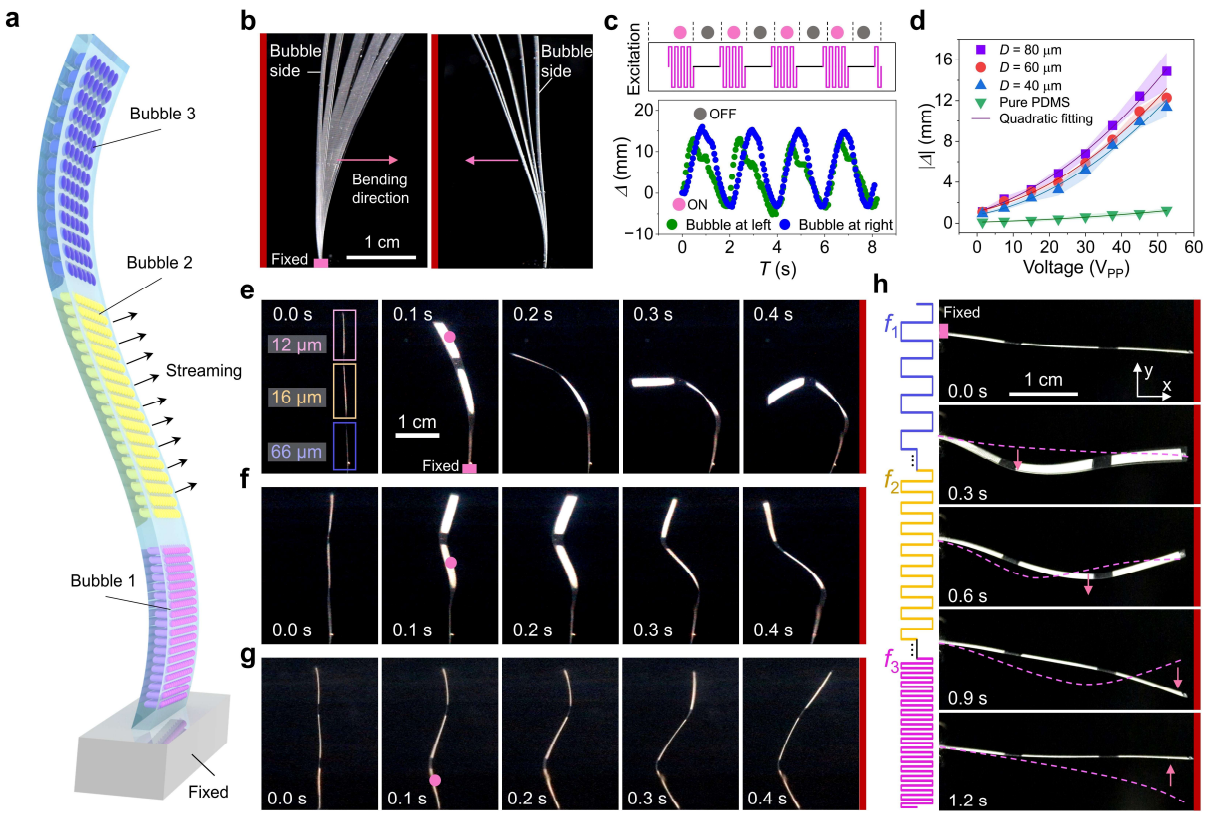


**Fig. 2. Actuation of microbubble-array artificial muscles. a**, Schematic of the variable-size microbubble array artificial muscle, composed of three different microbubble arrays. One end is fixed, while the other remains free. The yellow region is selectively excited to induce local deformation in the artificial muscle. **b**, Time-lapse images of a uniform-size microbubble array artificial muscle with microbubbles respectively positioned at the left and right side. The pink rectangle and arrow show the fixed end and bending direction of the muscle, respectively. The red line at the left side denotes the location of the transducer. **c**, Plot of the bending amplitude of the muscle tip over multiple excitation cycles with an average repeated-positioning error of ±0.8 mm with the excitation signal shown in the top panel. The pink and gray dots correspond to the excitation 'on' (80.5 kHz and 52.5 $V_{PP}$) and 'off' stages, respectively. The green and blue dots represent the measured deformation amplitudes when the bubbles are positioned on the left and

right sides, respectively, as shown in **b**. **d**, Bending amplitude of uniform-size microbubble array artificial muscles with microbubble diameters (*D*) of 40 μm, 60 μm, and 80 μm and without microbubbles under excitation voltages from 1.5 to 52.5 $V_{PP}$. The microbubbles have a constant depth of 50 μm. The dots and solid lines are the experimental results and quadratic fitting results, respectively. All the muscles bent in the direction as shown in the left panel of **b**. **e** to **g,** Time-lapse images of the individual deformation shapes of a variable-size microbubble array artificial muscle with microbubble diameters of 12 μm, 16 μm, and 66 μm. After 0.4 s the deformation will not change significantly. The microbubbles have a constant depth of 50 μm. The pink dots indicate the region of the bubble array that is activated. **h**, Time-lapse images of the variable-size microbubble array artificial muscle under sweeping-frequency ultrasound excitation (20-90 kHz, 1.2 s). The ultrasound excitation voltage for panels **e** to **h** was consistently at 60 $V_{PP}$. The artificial muscles utilized here are all measuring 3 cm in length, 0.5 cm in width, and 80 μm in thickness. The pink dashed lines mark the shape of the muscle at the previous time step, and the pink arrows mark the bending direction of the excited part.

**Programmable actuation of microbubble-array artificial muscles**

The versatility of microbubble arrays in terms of scalability, programmability, and selectivity enables an innovative approach for designing soft actuators with enhanced flexibility and control. To demonstrate this macroactuation, we designed a larger acoustic chamber (10 cm × 10 cm × 8 cm) filled with deionized water, with transducers mounted to its inner walls or freely put in the chamber (**Supplementary Fig. 4**). Multiple cameras positioned at different orientations captured the deformation dynamics of the artificial muscles from various angles. **Fig. 2a** illustrates the geometry and boundary conditions of a general artificial muscle. Further details on the acoustic setup are provided in the **Materials and Methods** section.

To determine the key factors influencing muscle deformation, a set of control experiments was performed. We first examined the streaming jets of a uniform-size microbubble array artificial muscle (1 cm × 0.3 cm × 80 μm) patterned with over 800 microcavities (each 40 μm in diameter and 50 μm in depth). **Supplementary Video 4** shows that an artificial muscle without microbubbles exhibited minor deformation, with no noticeable microstreaming observable across excitation frequencies sweeps from 1 to 100 kHz at 60 $V_{PP}$. When microbubbles were introduced into the actuator, they generated pronounced microstreaming near the bubbles (~0.8 mm/s) upon increased ultrasound stimulation frequency to 9.5 kHz, resulting in substantial deformation of the artificial muscle.

To verify that microbubble oscillation is the dominant driver of this muscle bending, we systematically varied the transducer's position relative to the microbubble-embedded side of the artificial muscle (3 cm × 0.5 cm × 80 μm), which contains over 10,000 uniform microbubbles within cavities (40 μm diameter, 50 μm depth). The transducer was positioned with four distinct orientations: (1) directly facing the microbubble-embedded side, (2) opposite to it, and (3-4) perpendicular to the array's left and right sides of the artificial muscle (**Fig. 2b**, **Supplementary Fig. 5**, and **Supplementary Video 5**). When activated at 80.5 kHz and 60 $V_{PP}$, the muscle consistently bent away in the direction opposite to the microbubble-array side, across all configurations, despite variations in bending amplitudes. This directional uniformity confirms that microbubble-generated reverse thrust is the primary force driving the deformation.

We then assessed the repeatability of the artificial muscle's deformation under identical excitation conditions. With the transducer close to the microbubble-embedded side, as shown in the left panel of **Fig. 2b**. When stimulated with ultrasound pulses (80.5 kHz, 60 $V_{PP}$, and 1 s on/off cycle), the muscle exhibited repeatable bending within 150 cycles, with an error of ±0.8 mm, representing 2.7% of the total beam length (**Fig. 2c**). With more excitation cycles (500 cycles) of the artificial muscle, the deformation exhibited larger error (~10%). After 10,000 cycles, there were no observable microbubbles in the artificial muscle, and the artificial muscle exhibited minor deformation. Furthermore, **Fig. 2d** reveals a quadratic relationship between the applied voltage and the mean deformation amplitude of artificial muscles patterned with microbubbles of various diameters (40 μm, 60 μm, and 80 μm) when driven at their respective resonance frequencies (80.5 kHz, 62.5 kHz, and 30.3 kHz). Additionally, the PDMS beam, in the absence of microbubbles, exhibited limited bending (~7% of the 40 μm microbubble-array artificial muscle's deformation at 60 $V_{PP}$) caused by the weak radiation force from incident sound waves originating from the transducer.

To demonstrate the selective excitation capability of the artificial muscle, we further investigated the deformation of an artificial muscle equipped with variable-size microbubble arrays. The muscle, measuring 3 cm × 0.5 cm × 80 μm, contains three arrays of microbubbles with diameters of 12, 16, and 66 μm, each with a depth of 50 μm. Upon stimulation at its resonance frequency (96.5 kHz), the 12 μm × 50 μm microbubble array, covering an area of 0.5 $cm^2$, induced a leftward deformation in the corresponding muscle region, as depicted in **Fig. 2e** and **Supplementary Video 6**. Similarly, when the frequency was respectively increased to match the resonance frequencies of the 16 μm (82.3 kHz, **Fig. 2f**) and 66 μm (33.2 kHz, **Fig. 2g**) bubble arrays, the muscle showed a localized leftward deformation in the middle region and bottom region, respectively. We further demonstrated an undulatory sinusoidal-like deformation by actuating the artificial muscle with a sweeping-frequency ultrasound excitation (20 to 90 kHz). This continuous, time-dependent motion, as shown in **Fig. 2h** and **Supplementary Video 7**, resulted from the periodic reverse thrust generated across different regions of the muscle. For each deformation, the excitation cycle was repeated more than ten times, and the average repeated-positioning error of the muscle tip was ±0.4 mm.

**Modeling of microbubble-array artificial muscles**

We have developed a theoretical model to improve our understanding of the response of soft artificial muscles to sound waves. This model divides the entire artificial muscle into discrete segments that correspond to the patterned microbubble arrays, as illustrated in **Fig. 3**. We began by modeling the acoustofluidic thrust force from a single trapped microbubble and analyzing the resulting artificial muscle deformation. To formulate the model, we assumed that (i) the ultrasound produces a homogeneous oscillating pressure field at the microbubble, generating the thrust force; (ii) the beam's oscillation amplitude is negligible compared to that of the microbubbles, such that its motion does not significantly affect the surrounding flow field; (iii) hydrodynamic coupling between oscillating microbubbles can be neglected; (iv) the acoustic streaming force is dominated; (v) beam stretching is negligible; and (vi) gravity of the muscle does not influence the beam deformation.

To calculate the thrust force arising from acoustic streaming generated by a single oscillating microbubble, we adopted a model developed by Spelman and Lauga[68,69]. With additional approximations (**Supplementary Note 1**), we derived an expression for the thrust force

$$F_i \approx \pi\rho\omega {R_{ci}}^3 v_i \,, \tag{1}$$

where $\rho$ is the fluid density, $\omega$ the ultrasound frequency, $R_{ci}$ the cavity radius in segment $i$, and $v_i$ the mean tangential velocity along the microbubble surface perpendicular to the beam, measured experimentally (**Extended Data Fig. 3**). For example, a microbubble with a 40 μm radius in water ($\rho$ = 1000 kg/m³), excited at 27.6 kHz with 60 $V_{PP}$, produced a measured velocity of $v_i$ = 2.5 mm/s, yielding a thrust force of $F_i$ = 13.9 nN according to Eq. (1). Scaling this to an array of approximately 18,000 uniformly sized microbubbles on a 30 mm × 5 mm artificial muscle yields a total force reaches up to 182 μN, corresponding to a force intensity of 1.21 μN/mm².

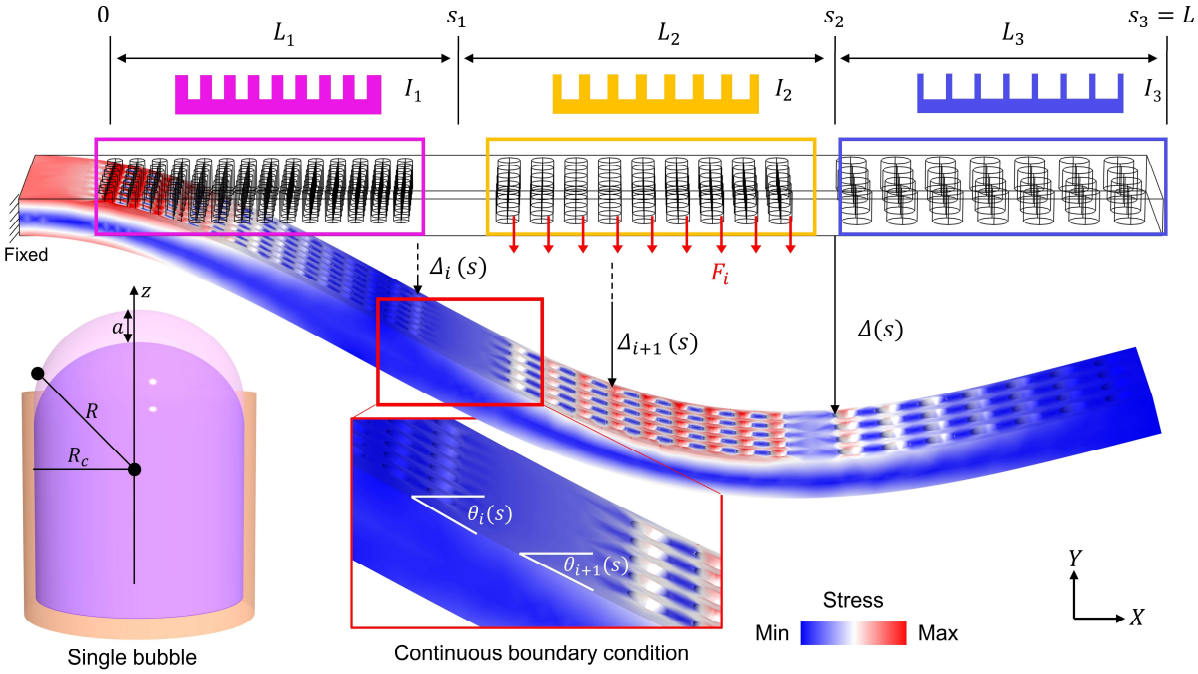


**Fig. 3 | Modeling of the activation mechanism of microbubble-array artificial muscles.** The pink, yellow, and blue boxes represent differently sized microbubble-array segments. The upper portion illustrates schematics of the cross-section of the artificial muscle, each corresponding to a specific second moment of area ($I$). The lower middle inset shows the continuous deformation conditions between different segments. $F_i$ denotes the thrust force generated by the microstreaming (here the yellow segment of the muscle generates thrust), $w_i$ and $\theta_i$ denote the deflection and rotation angle along the long axis ($Y$ axis). The lower left inset shows the modeling of a microbubble, where $R_c$ is the radius of the cavity, $R$ is the curvature radius of the trapped microbubble, and $a$ is the amplitude of the center displacement during oscillation.

To describe the beam deformation, we parameterized the slender beam length by a variable $s$. Owing to planar symmetry, the deformation is fully described by the local slope angle $\theta(s)$. Using linear elasticity and the known orthogonal thrust force density, we derived the governing equation for $\theta(s)$ (see **Supplementary Note 2**). Assuming small variations in $\theta$ within each segment, we obtained an analytical expression for $\theta(s)$ in terms of the beam's Young's modulus $E$, second moment of area $I$, and the segmental thrust force densities. The resulting $Y$-direction deformation as a function of $s$ in $i$-th segment is then given by

$$\Delta(s) = \sum_{i=1}^{N} \int_0^s \sin\big(\theta_i(s)\big)\, \mathrm{d}s\,. \tag{2}$$

Our model is applicable to artificial muscles featuring both uniform-size and variable-size microbubble arrays (**Supplementary Fig. 6**). The model demonstrates that the deformation amplitude of an artificial muscle can be amplified quadratically by increasing the ultrasound excitation voltage ($\Delta \propto V_{PP}^2$, as shown in **Supplementary Fig. 7**). Besides, the model shows that the deformation can be increased by increasing the number of microbubbles (**Supplementary Fig. 8**). Additionally, larger deformation can be achieved by either reducing the material's Young's modulus or decreasing the muscle's thickness (**Supplementary Fig. 9**). Furthermore, we envision that expanding the range of microbubble sizes enhances the manipulation freedom.

**Applications of microbubble-array artificial muscles**

The development of programmable microbubble-array artificial muscles presents an exciting alternative for wireless actuation, enabling innovative designs in the field of soft robotics. Trapping and manipulating small, fragile model animals (e.g., zebrafish embryos) could become an appealing area of research in soft robotics. Conventional micro-tweezers often lack sufficient gripping force, while bulkier grippers risk damaging delicate targets. To address this, we introduced and designed a miniaturized soft gripper comprised of six to ten uniform-size microbubble array artificial muscles, which are distributed in a manner resembling the petals of a flower, as illustrated in **Fig. 4a**. Each tentacle measures 10 mm in length, 0.7 mm in width, and 0.08 mm in thickness and together houses over 60,000 microbubbles (12 μm in diameter, 50 μm in depth) when submerged in water. In the absence of ultrasound, the flower-shaped gripper remains at rest in an open state. When subjected to an acoustic stimulus (95.5 kHz, 60 $V_{PP}$), it closes within 100 milliseconds and reopens when the stimulus is deactivated. The gripper demonstrated robust actuation across multiple positions and orientations in the acoustic tank, indicating the ability to be actuated independently of the position of the transducer (**Supplementary Video 8**).

To test its functionality, a zebrafish larva (1 mm in length, 300 μm in diameter) was released into the tank. Prior to ultrasound excitation, the larva swam freely around the gripper's tentacles. Upon ultrasound stimulation, the tentacles gripped the mobile larva. When the acoustic stimulus was deactivated, the larva easily swam away (**Supplementary Video 9**). Repeated actuation showed no notable heating or adverse effects on the larva, confirming the biocompatibility of the mechanism. Remarkably, the gripper can secure objects weighing 250 mg (i.e., 35 times its own weight of 7 mg) with potential force enhancement by incorporating additional microbubbles or tentacles (**Fig. 4b**). Further analysis highlighted the gripper's rapid response relative to the gripping ability (**Fig. 4c** and **Supplementary Table 1**) and a good force-to-weight ratio compared to its size (**Fig. 4d** and **Supplementary Table 2**).

We further demonstrated the artificial muscle as a conformable robotic skin capable of adhering to arbitrary surfaces and imparting motion to stationary objects. For example, upon switching on the ultrasound excitation (95.5 kHz and 60 $V_{PP}$), the robotic skin containing a uniform-size microbubble array (12 μm × 50 μm) self-adhered to a blade of grass and enabled it to bend (**Fig. 4e** and **Supplementary Video 10**). We also attached the robotic skin to an arbitrary-shaped almond that exhibited controllable counter-clockwise rotation upon excitation (**Fig. 4f** and

**Supplementary Video 11**). The microbubble-array robotic skin offers the inanimate object diverse mobilities without notable size or mass increase. These results highlight the potential for the future development of wireless and wearable devices based on this technology for human applications.

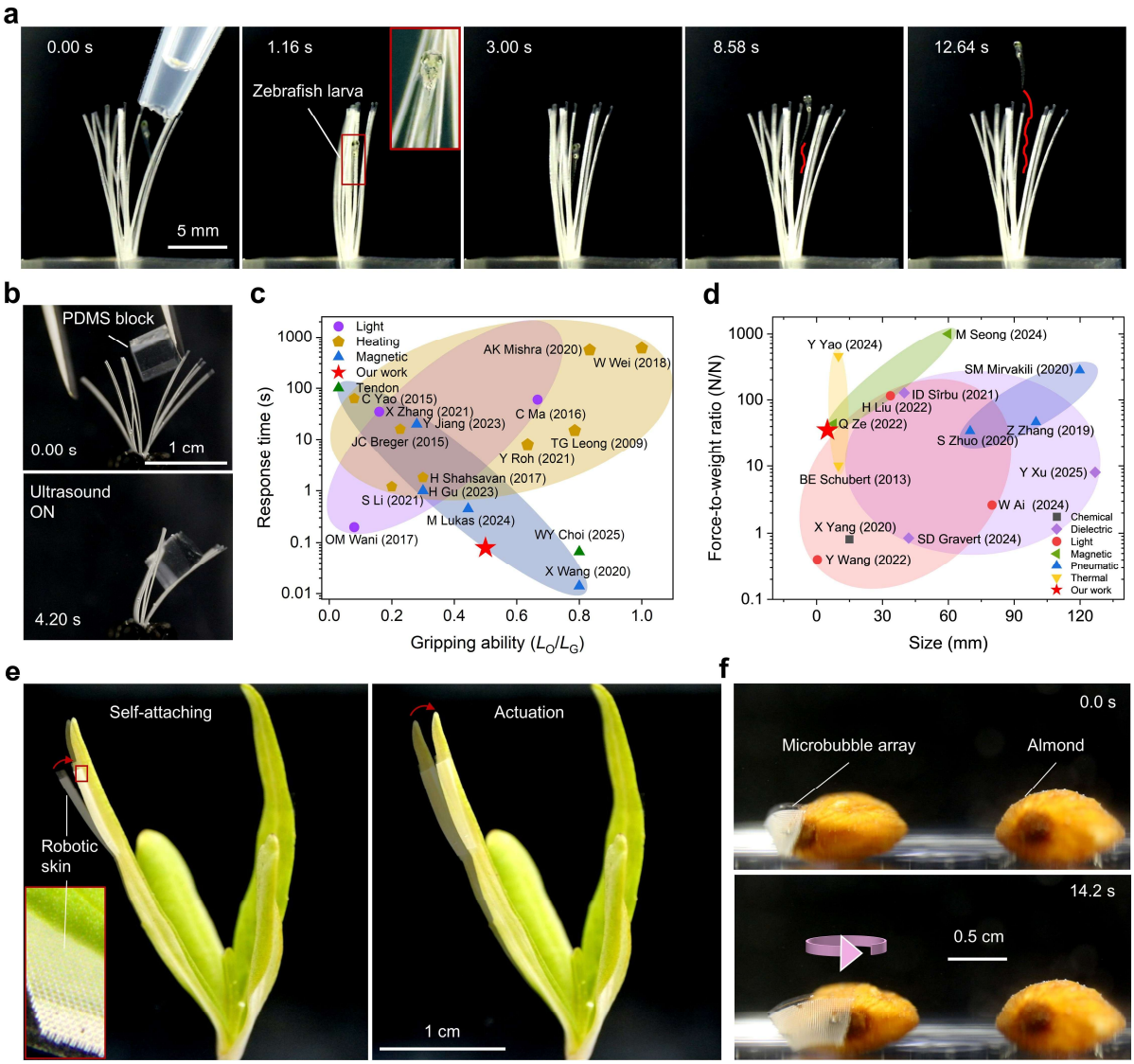


**Fig. 4 | Adaptive gripping and robotic skin applications of microbubble-array artificial muscles. a**, A live zebrafish larva trapped by a soft gripper featuring multiple microbubble-array artificial muscles as tentacles. The inset shows a zoom-in view of the larva. **b**, A soft gripper captured a PDMS block with 35 times of its own weight. **c**, Response time versus gripping ability ($L_O/L_G$) for grippers using different actuation methods, where $L_O$ and $L_G$ are the dimensions of the gripped object and gripper, respectively. **d**, Comparison of force-to-weight ratios of artificial muscles versus dimensions for various actuation methods. Shaded regions in **c** and **d** (convex hulls) indicate typical performance ranges; representative studies are labeled by author and year. **e**, Closing of a piece of grass and **f**, rotating of an almond by a conformable microbubble-array robotic skin. The inset shows a zoom-in view of the microbubble array.

Leveraging the precise selectivity and programmable deformation of the artificial muscle, we developed a multimodal shape transformer. As shown in **Fig. 5a**, a ring of functional surface with a diameter from 3 to 5 cm is patterned with six microbubble arrays with bubble diameters of 12 μm, 16 μm, and 66 μm and a depth of 50 μm, and topped with a circular PDMS block (2 cm diameter, 0.3 cm thickness) to reduce buoyancy. By individually applying ultrasound excitation frequencies of 96.2 kHz, 82.5 kHz, and 33.2 kHz, the surface shows selective multimodal deformation. Under a sweeping-frequency excitation from 10 to 100 kHz at 60 $V_{PP}$, the surface shows a counter-clockwise undulatory motion (**Fig. 5b** and **Supplementary Video 12**). The surface demonstrates the remote driving capability and tuning ability of the microbubble-array artificial muscles. We envision that by patterning more sizes of microbubbles and programming the ultrasound excitation frequency accordingly, the surface possesses significantly increasing modes of deformation.

Capitalizing on the dynamic deformation and rapid response capabilities of our artificial muscle, we engineered a bioinspired ultrasound-powered wireless stingraybot. The biomimetic stingraybot features two artificial muscles—designed to mimic the pectoral fins of a natural stingray—integrated on its sides. These pectoral fins incorporate arrays of differently sized microbubbles (12 μm, 16 μm, and 66 μm in diameter; 50 μm in depth) patterned along the head-to-tail axis and paired with a PDMS block for buoyancy adjustment. When exposed to a sweeping-frequency ultrasound stimulation (30 to 90 kHz over 2 s at 60 $V_{PP}$), the stingraybot's fins exhibit an undulatory motion that mimics the natural motion of a stingray (**Fig. 5c**, **Supplementary Video 13**). Upon release, the stingraybot propels forward at an initial speed of ~0.8 body lengths per second (**Fig. 5d)**, achieving competitive speeds compared to both micro- and macroscale robots using magnetic, electric, light, pressure, chemical, biohybrid, and other acoustically propelled microscale swimmers (**Fig. 5e** and **Supplementary Table 3**).

In control experiments, a stingraybot without microbubbles exhibited no undulatory motion along its fins under ultrasound excitation and sank without notable lateral displacement (**Supplementary Video 14**). Notably, under continuous single-frequency excitation (60 $V_{PP}$ at 33.2 kHz, 85.2 kHz, and 96.2 kHz) targeting distinct microbubble arrays (with diameters of 66 μm, 16 μm, and 12 μm, respectively), the stingraybot exhibited only limited locomotion (<1 body length). In comparison, sweeping-frequency excitation (10–100 kHz over 2 s) elicited sustained undulatory motion, allowing the stingraybot to swim a significantly greater distance (>3.5 body lengths), as shown in **Supplementary Fig. 10**. These results suggest that the forward motion of the stingraybot is predominant by the propulsion force generated by the sequential undulatory motion, resulting from the reverse thrust generated by microbubble arrays. Moreover, enhancing the design of the stingraybot with additional microbubble sizes could expand its maneuverability. For instance, integrating a navigation tail with microbubble arrays of different sizes on either side enables directional control. When activated at their respective resonance frequencies on one side, these arrays generate an asymmetric torque (**Supplementary Fig. 11**), enabling steer the stingraybot via tail rotation. Since the stingraybot is stealthy and transparent, we further envision that our stingraybot could be employed for environmental data collection or behavioral research on real organisms, for example, detecting water quality within coral reefs and recording swarm interaction by blending into schools of fish.

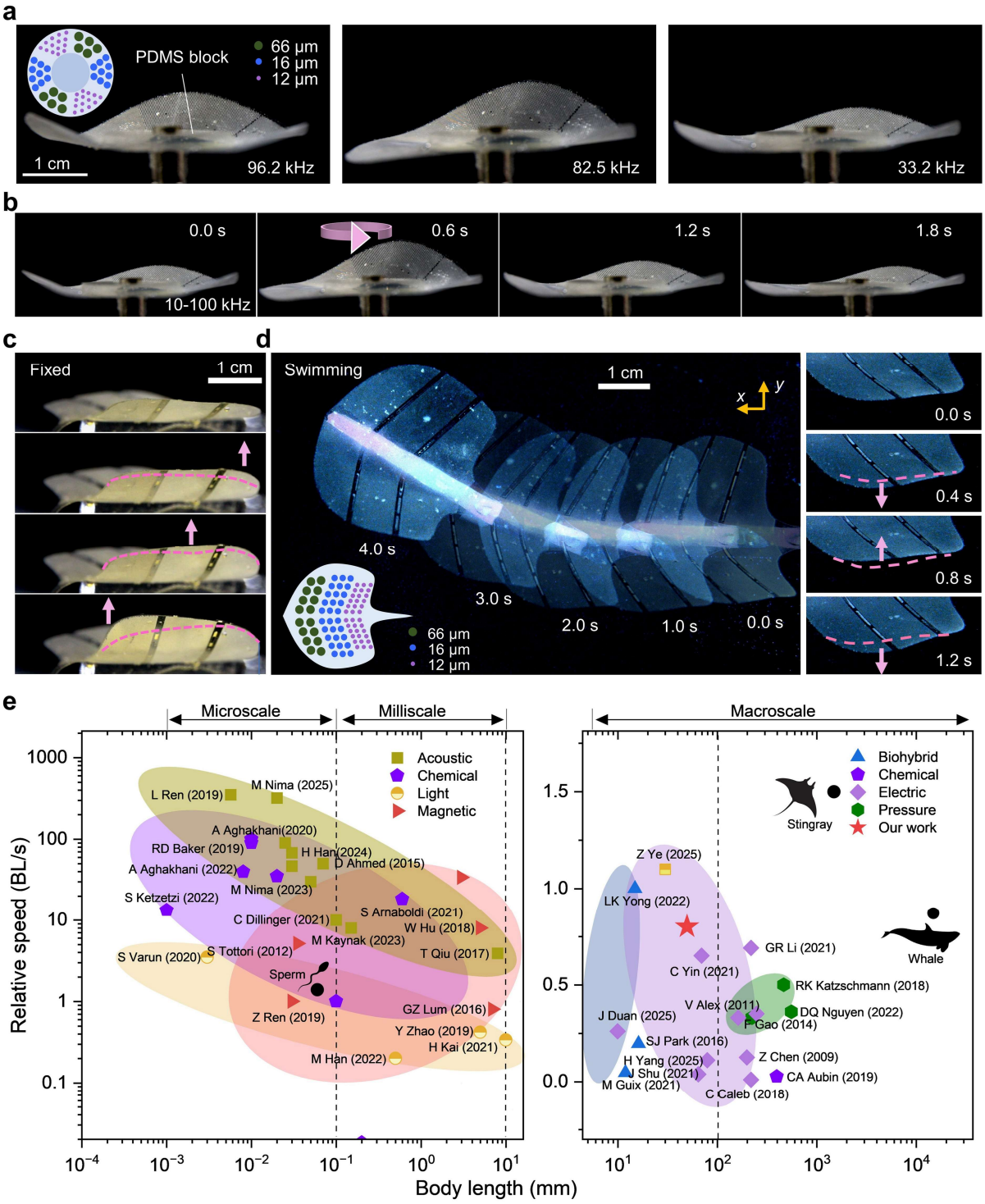


**Fig. 5 | Shape morphing and bioinspired swimming powered by microbubble-array artificial muscles. a**, Multimodal shape transformation of a circular surface under continuous ultrasound excitation frequencies of 96.2 kHz, 82.5 kHz, and 33.2 kHz, respectively. The circular surface was topped with a circular PDMS block (2 cm diameter, 0.3 cm thickness) to reduce buoyancy. The inset shows a schematic of the microbubble array patterned on the surface. **b**, Dynamic shape

transformation of the circular surface under sweeping-frequency ultrasound excitation spanning from 10 kHz to 100 kHz over 2 s. **c**, Undulation motion of the microbubble-array fins of the bioinspired stingraybot before releasing. **d**, Forward swimming of the stringraybot. The right panel displays the undulatory fin in motion during swimming, while the lower inset presents a schematic of the microbubble arrays patterned onto the fin. In **c** and **d**, the magenta dotted line and arrow respectively denote the shape of the fins in the last time step and the moving direction of the fins in the current time step. **e**, Comparison of relative swimming speeds (body lengths per second) of swimmers with different actuation mechanisms across various scales (microscale to macroscale). Shaded regions (convex hulls) indicate typical performance ranges; representative studies are labeled by author and year.

**Discussion**

We have introduced a new class of soft artificial muscles that utilize acoustically activated microbubble arrays to achieve programmable actuation. These acoustic artificial muscles exhibit dynamic programmability, high force intensity (~1.21 μN/mm$^2$), rapid responsiveness (sub-100 ms), and wireless controllability, all while maintaining exceptionally compact (3,000 microbubbles/mm$^2$) and lightweight (0.047 mg/mm$^2$). Through the strategic use of microbubble configurations and voltage and frequency as ultrasound excitation parameters, we engineered a diverse range of preprogrammed movements (e.g., undulatory motion) and demonstrated their applicability across artificial muscle platforms. We showcased the strength and durability of these muscles by integrating variable-size microbubble arrays into functional devices such as a soft gripper, a robotic skin, a shape transformer, and a biomimetic stingray robot. We also established a theoretical model that elucidates the actuation mechanism, which serves as a guide for the design of microbubble array patterns with enhanced actuation performance. These artificial muscles offer extensive applications in robotics, flexible electronics, wearables technologies, prosthetics, biomedical instrumentations, and beyond.

To evaluate the robustness of our ansatz, we studied the artificial muscle performance in various aqueous solutions (deionized water, tap water, and 25–100% glycerol solutions) as shown in **Extended Data Fig. 5**. The deformation exhibited an inverse relationship with glycerol concentration, with the largest deformation of ~11.3 mm in a 25% glycerol solution, followed by ~8.4 mm in 50% glycerol and 3.7 mm in 75% glycerol. The deformation was almost negligible in 100% glycerol. We next evaluated how solid media placement affects artificial muscle actuation (**Extended Data Fig. 6**). A frontal obstruction (partially blocking ultrasound) reduced the deformation by 80–90% (0.5–1 mm tip deformation versus 4.8 mm unobstructed). A lateral placement caused moderate attenuation (~2.5 mm), while posterior positioning retained a better performance (3.8 mm). Thus, actuators remained functional near obstacles but required strategic positioning to maximize deformation. Our preliminary results also revealed negligible heating effects near the piezoelectric transducer during artificial muscle and stingraybot operation (**Supplementary Fig. 12**), underscoring the thermally benign nature of this acoustic actuation platform.

Future work should focus on optimizing the artificial muscle performance through the geometric design and the density of the microcavities. Preliminary experiments revealed that converging trapezoidal cavities generate ~3× stronger streaming velocities than diverging shapes (**Extended Data Fig. 7**). We also conducted preliminary studies on the density of cavities embedded within an artificial muscle (**Supplementary Fig. 8)**. By incorporating geometric and density optimization

with systematic characterization, one can establish a predictive design framework for actuators with tailored deformation profiles—enabling precision control in applications from soft robotics to biomedical devices. Future studies could also explore the application of confocal sound sources, such as high-intensity focused ultrasound (**Supplementary Fig. 13**) to achieve local millimeter deformation—which potentially could lead to new tools for applications such as in vivo mechanotransduction and spatially targeted drug delivery.

Despite promising results, certain limitations remain. Prolonged actuation triggers microbubble growth within the cavities, destabilizing the muscle operation after ~30 minutes (**Supplementary Fig. 14**). Resubmersion in water restores the function, and sealing cavities with a thin PDMS membrane will offer a long-term robust solution (**Extended Data Fig. 8)**. Additionally, the stingraybot's distance-dependent actuation must be taken into account for untethered operation. Our preliminary experiments at varying transducer distances revealed deformation decays with increasing distance (**Supplementary Fig. 15**), dropping by ~50% at 5 cm compared to the deformation at 1 cm. While this limitation is less critical in vivo (where the robot is intended to operate in confined volumes, e.g., the bladder), optimizing the actuation voltage to compensate for ultrasound intensity decay over distance can enhance the performance.

Looking ahead, these artificial muscles hold transformative potential across cutting-edge fields such as soft robotics, haptic medical devices, and minimally invasive surgery. Future research should focus on refining the scalability of these systems across multiple scales (**Extended Data Fig. 9**), enhancing their force generation capabilities, and integrating them into complex devices for biomedical applications.

**Extended Data**
Extended Data Figs. 1 to 9

## References


1. Hill, A. V. The dimensions of animals and their muscular dynamics. *Sci. Prog.* **38**, 209–230 (1950).
2. Gordon, M. S. *et al. Animal locomotion: physical principles and adaptations* (CRC Press, 2017).
3. Li, M., Pal, A., Aghakhani, A., Pena-Francesch, A. & Sitti, M. Soft actuators for real-world applications. *Nat. Rev. Mater.* **7**, 235–249 (2022).
4. Zhang, J. *et al.* Robotic artificial muscles: current progress and future perspectives. *IEEE Trans. Robot.* **35**, 761–781 (2019).
5. Laschi, C., Mazzolai, B. & Cianchetti, M. Soft robotics: Technologies and systems pushing the boundaries of robot abilities. *Sci. Robot.* **1**, eaah3690 (2016).
6. Rus, D. & Tolley, M. T. Design, fabrication and control of soft robots. *Nature* **521**, 467–475 (2015).
7. Ortiz-Catalan, M. *et al.* A highly integrated bionic hand with neural control and feedback for use in daily life. *Sci. Robot.* **8**, eadf7360 (2023).
8. Kwak, J. W. *et al.* Wireless sensors for continuous, multimodal measurements at the skin interface with lower limb prostheses. *Sci. Transl. Med.* **12**, eabc4327 (2020).
9. Sanka, S. *et al.* A natural biomimetic prosthetic hand with neuromorphic tactile sensing for precise and compliant grasping. *Sci. Adv.* **11**, eadr9300 (2025).
10. Zhao, H., O'Brien, K., Li, S. & Shepherd, R. F. Optoelectronically innervated soft prosthetic hand via stretchable optical waveguides. *Sci. Robot.* **1**, eaai7529 (2016).
11. Zhou, S., Gao, X., Park, G. *et al.* Transcranial volumetric imaging using a conformal ultrasound patch. *Nature* **629**, 810–818 (2024).
12. Polygerinos, P., Wang, Z., Galloway, K. C., Wood, R. J. & Walsh, C. J. Soft robotic glove for combined assistance and at-home rehabilitation. *Rob. Auton. Syst.* **73**, 135–143 (2015).
13. Choi, W.-Y. *et al.* A hyperelastic torque-reversal mechanism for soft joints with compression-responsive transient bistability. *Sci. Robot.* **10**, eado7696 (2025).
14. Xie, Z. *et al.* Octopus-inspired sensorized soft arm for environmental interaction. *Sci. Robot.* **8**, eadh7852 (2023).
15. Cianchetti, M., Laschi, C., Menciassi, A. & Dario, P. Biomedical applications of soft robotics. *Nat. Rev. Mater.* **3**, 143–153 (2018).
16. Kim, Y., Parada, G. A., Liu, S. & Zhao, X. Ferromagnetic soft continuum robots. *Sci. Robot.* **4**, eaax7329 (2019).
17. Lacour, S. P., Courtine, G. & Guck, J. Materials and technologies for soft implantable neuroprostheses. *Nat. Rev. Mater.* **1**, 16063 (2016).
18. Joo, H. *et al.* Soft implantable drug delivery device integrated wirelessly with wearable devices to treat fatal seizures. *Sci. Adv.* **7**, eabd4639 (2021).
19. Roche, E. T. *et al.* Soft robotic sleeve supports heart function. *Sci. Transl. Med.* **9**, eaaf3925 (2017).
20. Davies, J. *et al.* Soft robotic artificial left ventricle simulator capable of reproducing myocardial biomechanics. *Sci. Robot.* **9**, eado4553 (2024).
21. Carton, M. *et al.* Bridging hard and soft: mechanical metamaterials enable rigid torque transmission in soft robots. *Sci. Robot.* **10**, eads0548 (2025).
22. Wang, Z., Freris, N. M. & Wei, X. SpiRobs: logarithmic spiral-shaped robots for versatile grasping across scales. *Device* **100646** (2024).
23. Buchner, T. J. K. *et al.* Vision-controlled jetting for composite systems and robots. *Nature* **623**, 522–530 (2023).
24. Pikul, J. H. *et al.* Stretchable surfaces with programmable 3D texture morphing for synthetic camouflaging skins. *Science* **358**, 210–214 (2017).
25. Aubin, C. A. *et al.* Powerful, soft combustion actuators for insect-scale robots. *Science* **381**, 1212–1217 (2023).
26. Xin, C. *et al.* Environmentally adaptive shape-morphing microrobots for localized cancer cell treatment. *ACS Nano* **15**, 18048–18059 (2021).
27. Miskin, M. Z. *et al.* Electronically integrated, mass-manufactured, microscopic robots. *Nature* **584**,

557–561 (2020).
28. Kollipara, P. S., Li, X., Li, J. *et al.* Hypothermal opto-thermophoretic tweezers. *Nat. Commun.* **14**, 5133 (2023).
29. Kim, I. H. *et al.* Human-muscle-inspired single fibre actuator with reversible percolation. *Nat. Nanotechnol.* **17**, 1198–1205 (2022).
30 Han, M. *et al.* Submillimeter-scale multimaterial terrestrial robots. *Sci. Robot.* **7**, eabn0602 (2022).
31. Li, M., Tang, Y., Soon, R. H., Dong, B., Hu, W. & Sitti, M. Miniature coiled artificial muscle for wireless soft medical devices. *Sci. Adv.* **8**, eabm5616 (2022).
32. Pang, W. *et al.* A soft microrobot with highly deformable 3D actuators for climbing and transitioning complex surfaces. *Proc. Natl Acad. Sci. USA* **119**, e2215028119 (2022).
33. Hwang, D., Barron, E. J., Haque, A. B. M. T. & Bartlett, M. D. Shape morphing mechanical metamaterials through reversible plasticity. *Sci. Robot.* **7**, eabg2171 (2022).
34. Bai, Y. *et al.* A dynamically reprogrammable surface with self-evolving shape morphing. *Nature* **609**, 701–708 (2022).
35. Ko, J. *et al.* High-performance electrified hydrogel actuators based on wrinkled nanomembrane electrodes for untethered insect-scale soft aquabots. *Sci. Robot.* **7**, eabo6463 (2022).
36. Li, G. *et al.* Self-powered soft robot in the Mariana Trench. *Nature* **591**, 66–71 (2021).
37. Wang, X. *et al.* Untethered and ultrafast soft-bodied robots. *Commun. Mater.* **1**, 67 (2020).
38. Gu, H. *et al.* Self-folding soft-robotic chains with reconfigurable shapes and functionalities. *Nat. Commun.* **14**, 1263 (2023).
39. Kim, Y., Yuk, H., Zhao, R., Chester, S. A. & Zhao, X. Printing ferromagnetic domains for untethered fast-transforming soft materials. *Nature* **558**, 274–279 (2018).
40. Ren, Z., Hu, W., Dong, X. & Sitti, M. Multi-functional soft-bodied jellyfish-like swimming. *Nat. Commun.* **10**, 2703 (2019).
41. Nelson, B. J. & Pané, S. Delivering drugs with microrobots. *Science* **382**, 1120–1122 (2023).
42. Overchuk, M. *et al.* Photodynamic and photothermal therapies: synergy opportunities for nanomedicine. *ACS Nano* **17**, 7979–8003 (2023).
43. Mao, L., Yang, P., Tian, C. *et al.* Magnetic steering continuum robot for transluminal procedures with programmable shape and functionalities. *Nat. Commun.* **15**, 3759 (2024).
44. Ozcelik, A. *et al.* Acoustic tweezers for the life sciences. *Nat. Methods* **15**, 1021–1028 (2018).
45. Zhang, Z., Shi, Z. & Ahmed, D. SonoTransformers: transformable acoustically activated wireless microscale machines. *Proc. Natl. Acad. Sci. USA* **121**, e2314661121 (2024).
46. Del Campo Fonseca, A. *et al.* Ultrasound trapping and navigation of microrobots in the mouse brain vasculature. *Nat. Commun.* **14**, 5889 (2023).
47. Deng, Y., Paskert, A., Zhang, Z., Wittkowski, R. & Ahmed, D. An acoustically controlled helical microrobot. *Sci. Adv.* **9**, eadh5260 (2023).
48. Marzo, A. & Drinkwater, B. W. Holographic acoustic tweezers. *Proc. Natl Acad. Sci. USA* **116**, 84–89 (2019).
49. Zhang, Z., Sukhov, A., Harting, J., Malgaretti, P. & Ahmed, D. Rolling microswarms along acoustic virtual walls. *Nat. Commun.* **13**, 7347 (2022).
50. Dillinger, C., Nama, N. & Ahmed, D. Ultrasound-activated ciliary bands for microrobotic systems inspired by starfish. *Nat. Commun.* **12**, 6455 (2021).
51. Durrer, J. *et al.* A robot-assisted acoustofluidic end effector. *Nat. Commun.* **13**, 6370 (2022).
52. Jooss, V. M., Bolten, J. S., Huwyler, J. & Ahmed, D. In vivo acoustic manipulation of microparticles in zebrafish embryos. *Sci. Adv.* **8**, eabm2785 (2022).
53. Han, H. *et al.* Imaging-guided bioresorbable acoustic hydrogel microrobots. *Sci. Robot.* **9**, eadp3593 (2024).
54. Goyal, R. *et al.* Amplification of acoustic forces using microbubble arrays enables manipulation of centimetre-scale objects. *Phys. Rev. Lett.* **128**, 254502 (2022).
55. Dolev, A., Kaynak, M. & Sakar, M. S. Dynamics of entrapped microbubbles with multiple openings. *Phys. Fluids* **34**, 012003 (2022).

56. Lajoinie, G., Luan, Y., Gelderblom, E. *et al.* Non-spherical oscillations drive the ultrasound-mediated release from targeted microbubbles. *Commun. Phys.* **1**, 22 (2018).
57. Ahmed, D., Lu, M., Nourhani, A. *et al.* Selectively manipulable acoustic-powered microswimmers. *Sci. Rep.* **5**, 9744 (2015).
58. Mahkam, N. *et al.* Multiorifice acoustic microrobot for boundary-free multimodal 3D swimming. *Proc. Natl Acad. Sci. USA* **122**, e2417111122 (2025).
59. Ahmed, D. *et al.* Artificial acousto-magnetic soft microswimmers. *Adv. Mater. Technol.* **2**, 1700050 (2017).
60. Ren, L. *et al.* 3D steerable, acoustically powered microswimmers for single-particle manipulation. *Sci. Adv.* **5**, eaax3084 (2019).
61. Aghakhani, A., Yasa, O., Wrede, P. & Sitti, M. Acoustically powered surface-slipping mobile microrobots. *Proc. Natl Acad. Sci. USA* **117**, 3469–3477 (2020).
62. Kaynak, M., Dolev, A. & Sakar, M. S. 3D printed acoustically programmable soft microactuators. *Soft Robot.* **10**, 246–257 (2023).
63. Qiu, T., Palagi, S., Mark, A. G., Melde, K., Adams, F. & Fischer, P. Wireless actuation with functional acoustic surfaces. *Appl. Phys. Lett.* **109**, 191602 (2016).
64. Qiu, T. *et al.* Wireless acoustic-surface actuators for miniaturized endoscopes. *ACS Appl. Mater. Interfaces* **9**, 42536–42543 (2017).
65. Wu, H. *et al.* Effects of surface tension on the dynamics of a single microbubble near a rigid wall in an ultrasonic field. *Ultrason. Sonochem.* **78**, 105735 (2021).
66. Khismatullin, D. B. Resonance frequency of microbubbles: effect of viscosity. *J. Acoust. Soc. Am.* **116**, 1463–1473 (2004).
67. Oguz, H. N. & Prosperetti, A. The natural frequency of oscillation of gas bubbles in tubes. *J. Acoust. Soc. Am.* **103**, 3301–3308 (1998).
68. Bertin, N. *et al.* Propulsion of bubble-based acoustic microswimmers. *Phys. Rev. Appl.* **4**, 064012 (2015).
69. Spelman, T. A. & Lauga, E. Arbitrary axisymmetric steady streaming: flow, force and propulsion. *J. Eng. Math.* **105**, 31–65 (2017).

## Materials and Methods

### 1. Fabrication of artificial muscles

The negative patterns of artificial muscles are first designed in the commercial electronic design automation software (as shown in **Supplementary Fig. 1**). The patterns are transferred into a photomask by a direct writing laser (DWL2000) machine in a cleaning room (BRNC, Ruschlikon, Switzerland). Then, we spin coat the negative photoresist SU8-3025 on a 4-inch silicon wafer. By the standard lithographic fabrication, the patterns are transferred to the photoresist via exposing to UV light through the mask. After the developing process, the negative patterns of the microbubble arrays, i.e., micropillars, are additive on the wafer. The height of the micropillar depends on the spinning speed. Next, to enhance surface properties, a silane-based hydrophobic treatment was applied to the 4-inch wafer with micropillars for 1 hour (see fabrication flow at **Supplementary Fig. 16**). The PDMS (polydimethylsiloxane) used in this process was prepared with a 10:1 ratio of base to curing agent. Then, the PDMS mixture was poured onto the wafer. To ensure a high-quality coating, the mixture was degassed under vacuum pressure of less than 1 mBar. After degassing, spin-coating was performed on the wafer. Different spin speeds result in varying PDMS membrane thicknesses (**Extended Data Fig. 1**). After spin-coating, the PDMS was vacuumed again and cured in a sequential heating process: 1 hour at 60°C, followed by 1 hour at 80°C, and finally 1 hour at 100°C. Finally, the PDMS soft membrane was cured and ripped off from the wafer. This process yielded a uniform PDMS layer suitable for use in artificial muscle and soft robotics applications. In all our experiments, each cavity consistently trapped only a single bubble as the artificial muscle submerged into the water (**Supplementary Fig. 17**).

### 2. Acoustic setup

For the microscale characterization of microbubbles, the experimental setup is built on a thin glass substrate with dimensions of 24 mm × 60 mm × 0.18 mm. As shown in **Supplementary Fig. 2a**, a circular piezoelectric transducer (27 mm × 0.54 mm, resonance frequency 4.6 kHz ± 4%, Murata 7BB-27-4L0) is affixed to the glass substrate using an epoxy resin (2-K-Epoxidkleber, UHU Schnellfest). A square PDMS acoustic chamber (10 mm × 10 mm × 5 mm) is positioned in the front of the transducer, which is filled with deionized water and covered with a cover glass (22 mm × 22 mm × 0.18 mm). The substrate is then mounted on an inverted microscope (Axiovert 200M, ZEISS). For the macroscale actuation of artificial muscles by sound, the experimental setup is built on a plastic tank with dimensions of 10 cm × 10 cm × 8 cm and a thickness of 2 mm. As shown in **Supplementary Fig. 4a**, the circular piezoelectric transducers are affixed to the inside surfaces and the bottom surface of the tank using the epoxy resin or directly submerged into the liquid because the deionized water filled in the tank is not conductive. Three cameras are placed around the tank to capture the actuation of acoustic artificial muscles from multiple view angles. An electronic function generator (AFG-3011C, Tektronix) and an amplifier (0 − 60 $V_{PP}$, 15x amplification, High Wave 3.2, Digitum-Elektronik) are connected to the transducer to generate sound waves with tunable excitation frequencies and voltages.

### 3. Numerical simulations

Finite element numerical simulations are conducted using the commercial COMSOL Multiphysics software (v6.1, Burlington, MA), including simulations on the acoustic pressure field in the small PDMS chamber, acoustic streaming generated by variable-size microbubbles in the small PDMS chamber, the acoustic pressure field in the big acoustic tank, and the deformations of the artificial muscle. All simulations are performed with dimensions and material properties consistent with the

experiments. Physics modules of simulations on acoustic pressure include the solid mechanics, electrostatics, pressure acoustics fields, creeping flow, and heat transfer in solids and fluids. Simulations on the deformations of artificial muscles are performed using the solid mechanics module with corresponding boundary conditions and force conditions. The microstreaming-generated thrust is assumed to be a point force which is loaded on the bottom of each microcavity. Additionally, numerical calculations based on the theoretical model are performed using the commercial Matlab software (R2022b). See **Supplementary Notes** for simulation details.

**4. Imaging and analysis**

The microscale characterization of microbubbles is recorded with a high-speed camera (Chronos 1.4, Kron Technologies) attached to the inverted microscope. Recording frame rates range from 1069 to 32,668 frames per second (fps). The macroscale motion of ultrasound artificial muscles is recorded with a high-sensitive camera (Canon 6D and 24−70 mm camera lens, Canon). The recording frame rate is 50 fps. Recorded footages are analyzed in ImageJ.

**Acknowledgments:** D.A. was funded by the European Research Council (ERC) under the European Union's Horizon 2020 research and innovation program (grant agreement No. 853309, SONOBOTS); the Swiss National Science Foundation (SNSF) through the SNSF Project funding MINT 2022 (grant agreement No. 213058), Spark Grant (grant agreement No. 221285); and the ETH Research Grant (grant agreement No. ETH-08 20-1). Z.S. acknowledges financial support from the China Scholarship Council (202106320193). Z.Z. acknowledges financial support from the China Scholarship Council (202006210065). N.N. acknowledges the funding from the United States National Science Foundation (OIA-2229636, CBET-2407937). R.W. is funded by the Deutsche Forschungsgemeinschaft (DFG, German Research Foundation) — 535275785. We thank the operational team of the clean room facility in the Binnig and Rohrer Nanotechnology Center (BRNC) for their helpful discussion on the fabrication wafer. The authors thank Dan Schoenenberger for his helpful contribution to the initial fabrication and testing.

**Author contributions:** D.A. conceived and supervised the project. R.W. supervised J.S.. Z.Z., Z.S., and D.A. contributed to the designs of the actuator and soft robots. Z.S. and Z.Z. developed the fabrication of prototypes, performed experiments and data analysis. S.C.F.N. provided the zebrafish embryos and provided guidance on the zebrafish experiments. R.W., N.N., J.S., Z.S., Z.Z., and D.A. contributed to the theoretical understanding. J.S. provided the analytical derivations on the acoustofluidic thrust force and the beam deformation. Z.S. contributed to the numerical simulations. Z.Z., Z.S., R.W., J.S., N.N., and D.A. contributed to the scientific presentation, discussion, manuscript revision, and data analysis.

**Competing interests:** The authors declare that they have no competing interests.

**Data and materials availability:** All data needed to evaluate the conclusions in the paper are present in the paper and/or the Supplementary Materials.

**Extended Data**

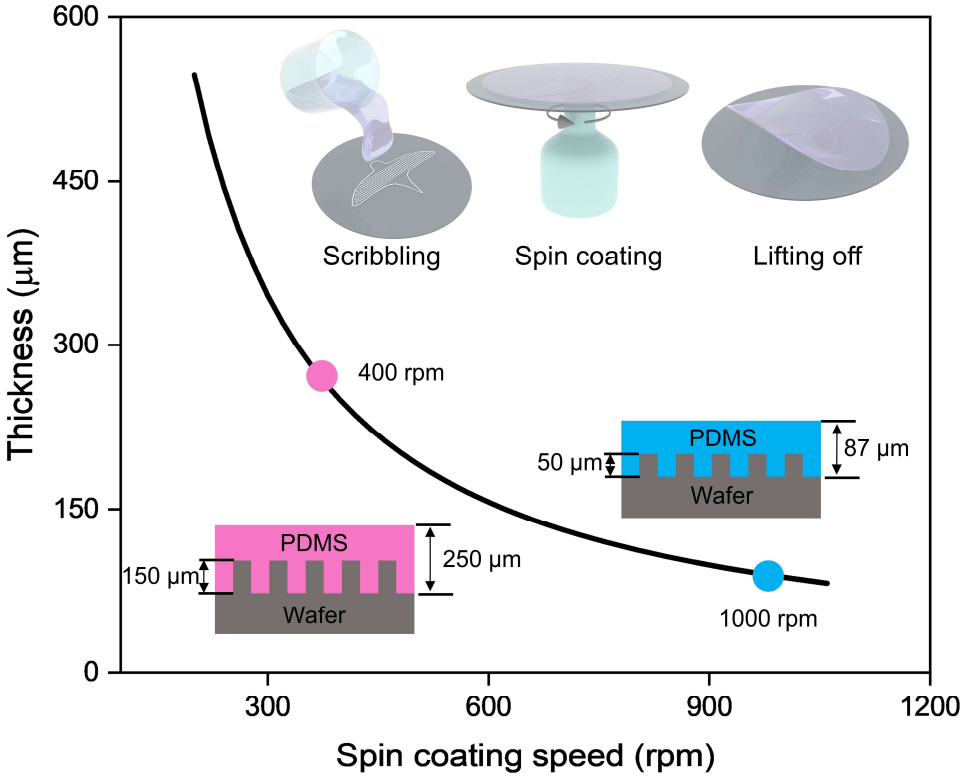


**Extended Data Fig. 1 | Artificial muscle thickness versus PDMS spin coating speed.** The black curve illustrates that the resulting thickness of the artificial muscle decreases with a higher spinning speed. The spinning speeds utilized in experiments are highlighted by two specific data points: The pink dot corresponds to a spinning speed of 400 rpm, which was employed on a wafer with 150 µm pillars, resulting in a thicker thickness of 250 µm for the artificial muscle. The blue dot represents a spinning speed of 1000 rpm, which was applied to a wafer with 50 µm pillars, yielding a thinner artificial muscle with a thickness of 87 µm. Insets demonstrate the fabrication process.

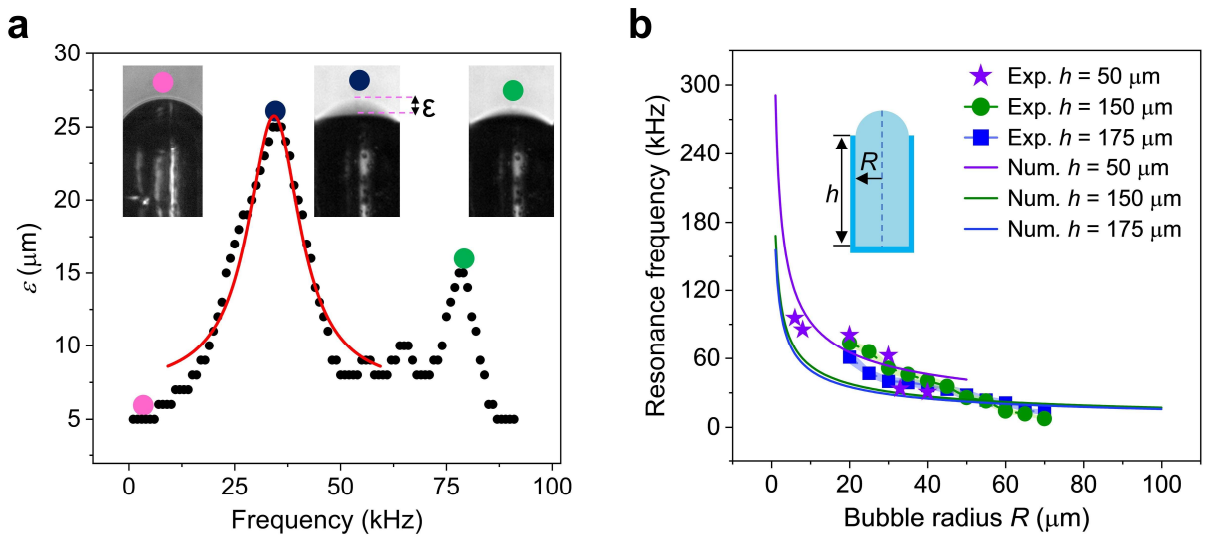


**Extended Data Fig. 2 | Characterization of the resonance frequency of different sized microbubbles. a**, Oscillation amplitude of a 60 μm × 150 μm microbubble as a function of the ultrasound excitation frequency. According to the measured oscillation amplitude of the microbubbles, the resonance frequency is identified to be 35.5 kHz. **b**, Experimentally measured resonance frequencies of microbubbles with depths of 150 μm and 175 μm, radii ranging from 20 to 70 μm in 5 μm increments, and a depth of 50 μm with radii of 6 μm, 8 μm, 20 μm, 30 μm, 33 μm and 40 μm. The solid lines represent numerically predicted results. Additionally, notable discrepancies exist between the calculated and measured resonance frequencies, which may originate from transducer coupling with the glass slide, interactions between bubbles, or other factors.

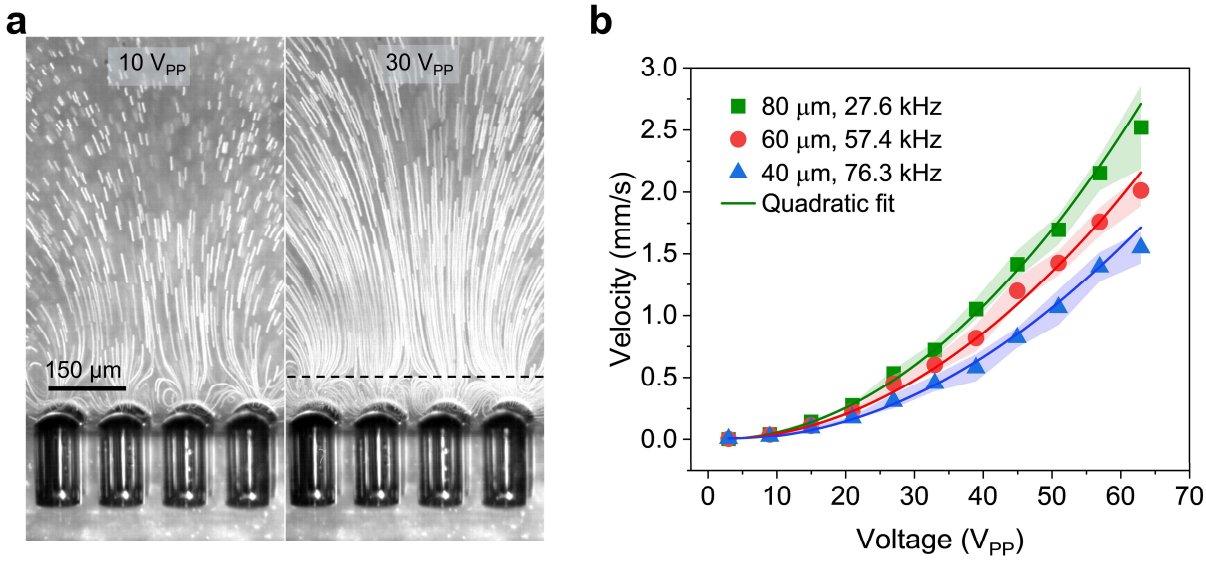


**Extended Data Fig. 3 | Measurement of microstreaming velocity by PIV. a**, Microstreaming generated by a 4×4 80 μm × 150 μm microbubble array under an excitation frequency of 27.6 kHz and two different voltages of 10 $V_{PP}$ (left panel) and 30 $V_{PP}$ (right panel). The black dotted line denotes the measurement position of the microstreaming velocity, which is 80 μm away from the surface. **b**, Plot of microstreaming velocity versus ultrasound excitation voltage respectively measured by 4×4 microbubble arrays with three different sizes (40 μm, 60 μm, and 80 μm). The solid lines are the quadratic fitting results.

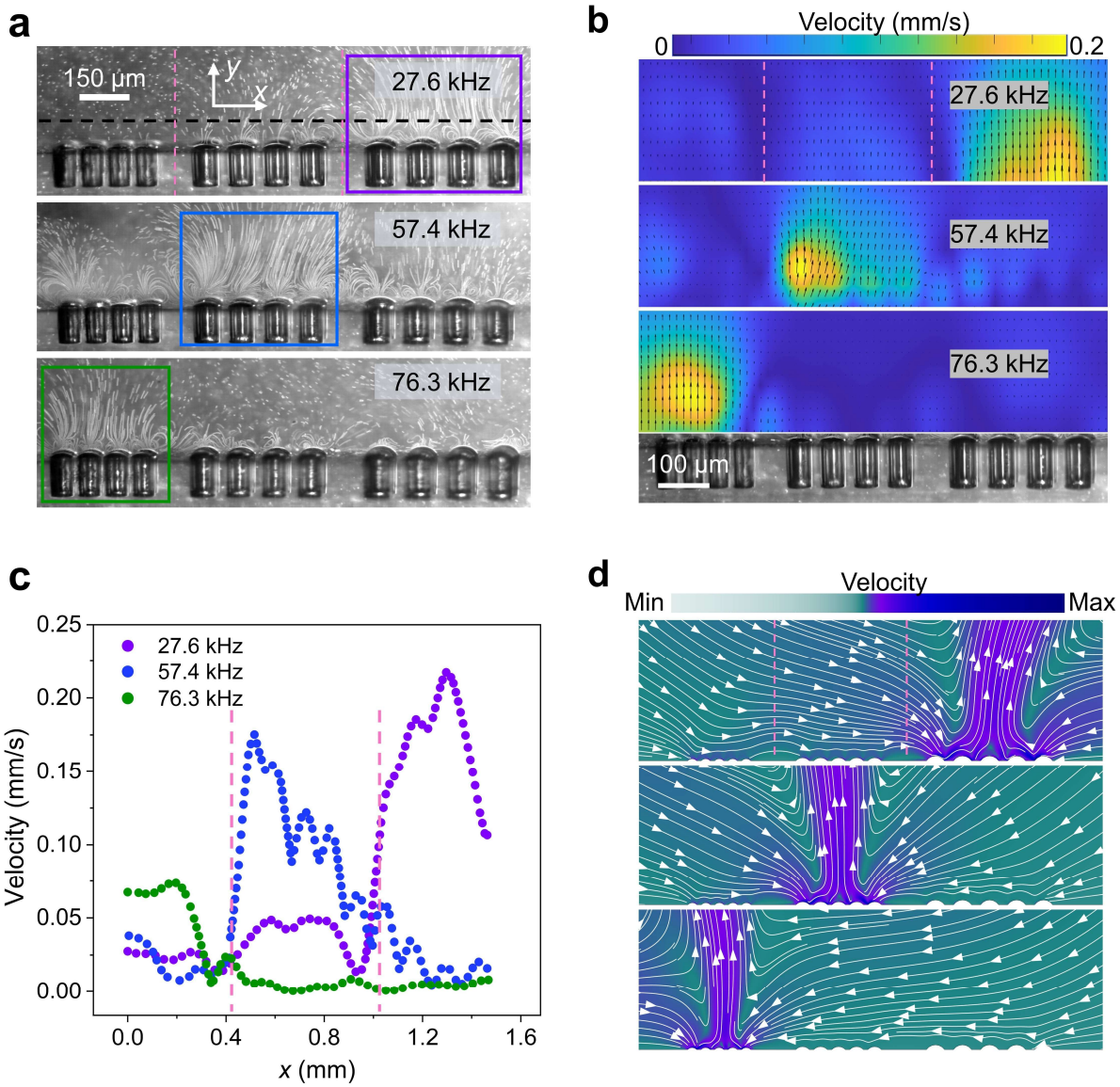


**Extended Data Fig. 4 | Selective actuation of microbubble arrays**. **a**, Microstreaming respectively generated by (40 μm, 60 μm, and 80 μm) microbubble arrays under ultrasound frequencies of 76.3 kHz (green), 57.4 kHz (blue), and 27.6 kHz (purple). Colored boxes indicate the activated microbubbles. The black dotted line denotes the measurement position of the microstreaming velocity, which is 100 μm away from the surface. **b**, Measured streaming flow of **a** with 2 μm trace microparticles. The streaming flow field was analyzed by PIV (Matlab R2022b, PIVlab 2.60). The color bar denotes the particle moving velocity perpendicular to and extending away from the bubble surface. **c**, Plot of the measured microstreaming velocity along the long axis of the variable-size microbubble array under different excitation frequencies. **d**, Simulations of microstreaming around the bubble array with three different excitation frequencies. The pink dotted lines in **a**, **b**, **c**, and **d** delineate the boundaries of three distinct microbubble arrays.

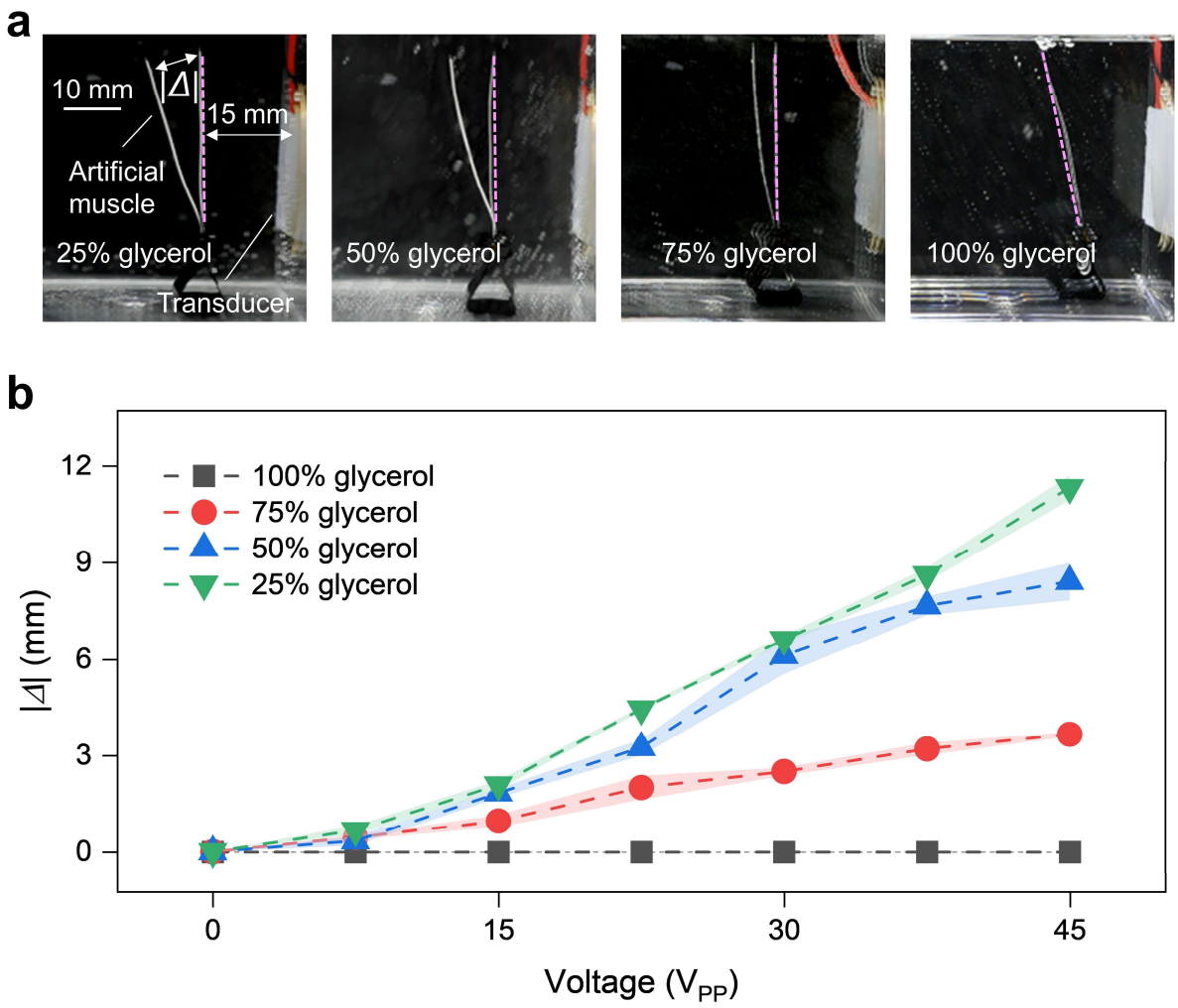


**Extended Data Fig. 5 | Deformation of an artificial muscle in liquid within different ratios of glycerol. a**, Experimental results for a uniform-size microbubble array artificial muscle (12 μm × 50 μm) under varying glycerol-water ratios. The distance between the transducer and the artificial muscle is 15 mm. Pink dashed lines indicate the initial position of the artificial muscle. Excitation was applied at 96.2 kHz with a voltage of 45 $V_{PP}$. **b**, Deformation ($|\Delta|$) of the artificial muscle as a function of the excitation amplitude for different glycerol-water ratios.

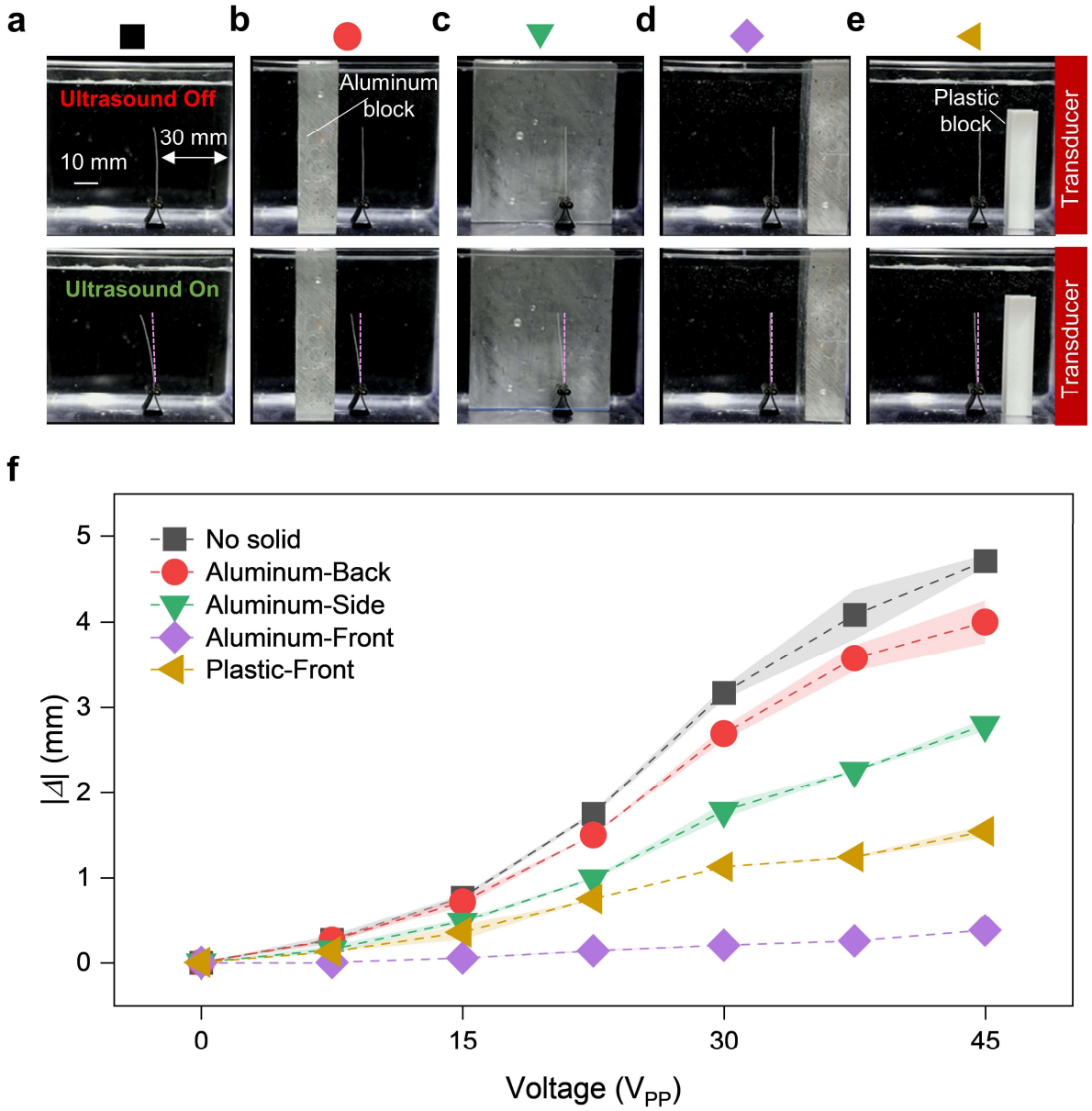


**Extended Data Fig. 6 | Effect of surrounding solid media on artificial muscle deformation under ultrasound excitation. a-e**, Experimental setup showing initial (pink dashed lines) and deformed positions of a uniform-size microbubble array artificial muscle (12 μm × 50 μm) with various solid-media configurations: no solid (black square), aluminum at the back (red circle), side (green triangle), and front (purple diamond), and plastic at the front (yellow triangle). All solids are placed 10 mm from the muscle, with the transducer 30 mm away. Excitation was applied at 95.5 kHz with a voltage of 45 $V_{PP}$. **f**, Deformation ($|\Delta|$) of the artificial muscle as a function of the excitation voltage for different solid media types and positions.

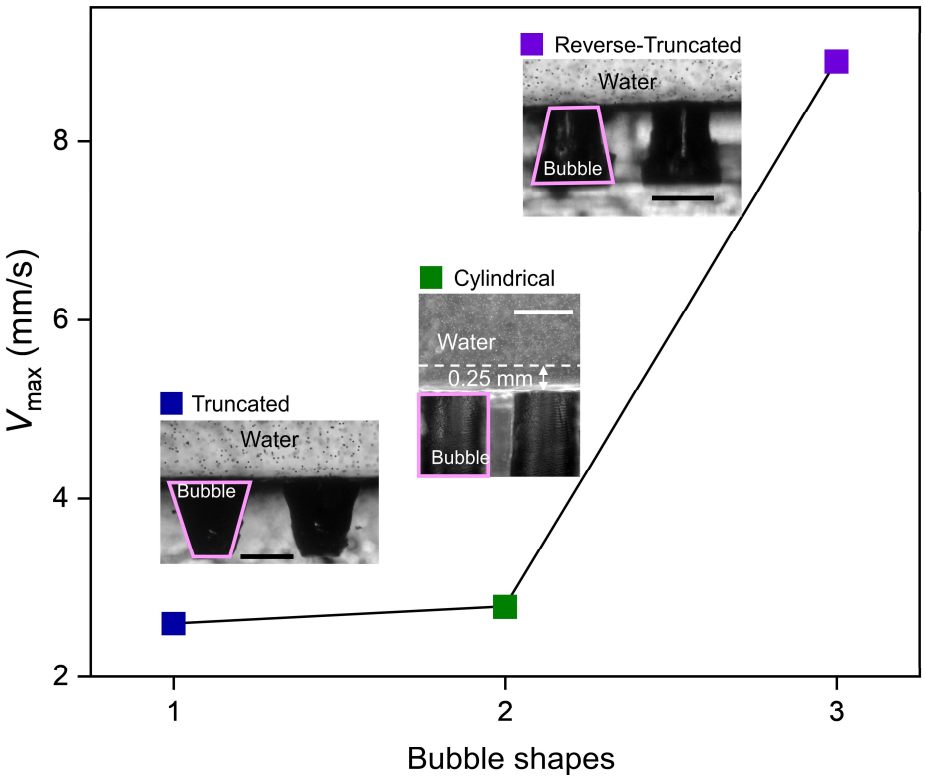


**Extended Data Fig. 7 | Measured maximum streaming of three different bubble shapes.** The blue, green, and purple points denote truncated, cylindrical, and reverse-truncated bubble shapes, respectively, with velocity measured along a line 0.25 mm from the bubble surface and 2 μm trace microparticles at 2.1 kHz and 30 $V_{PP}$ in all experiments. Scale bar: 1 mm.

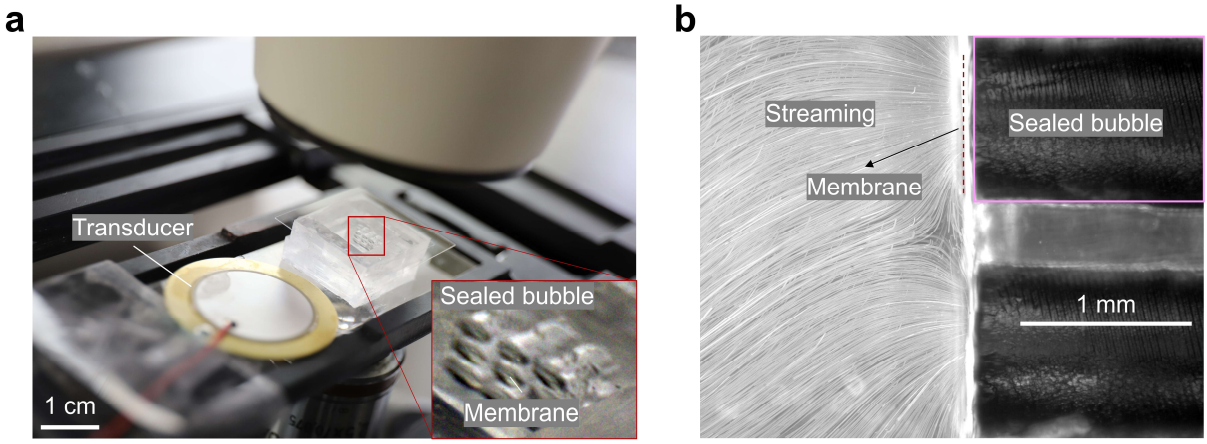


**Extended Data Fig. 8 | Experimental setup and streaming of membrane-sealed bubbles. a**, Experimental setup showing the transducer and a membrane-sealed 3 × 3 bubble array (1 mm diameter, 1.5 mm depth) mounted on a glass slide. The inset highlights the sealed bubbles. The membrane is 10 μm thick. **b**, Leftward microstreaming jetting generated from a microbubble array oscillating under ultrasound excitation demonstrated by 6 μm tracer microparticles. Excitation was applied at 2.1 kHz with a voltage of 60 $V_{PP}$. Pink rectangular represent the contour of the cross section of the sealed bubble, red dashed line indicates the location of the membrane.

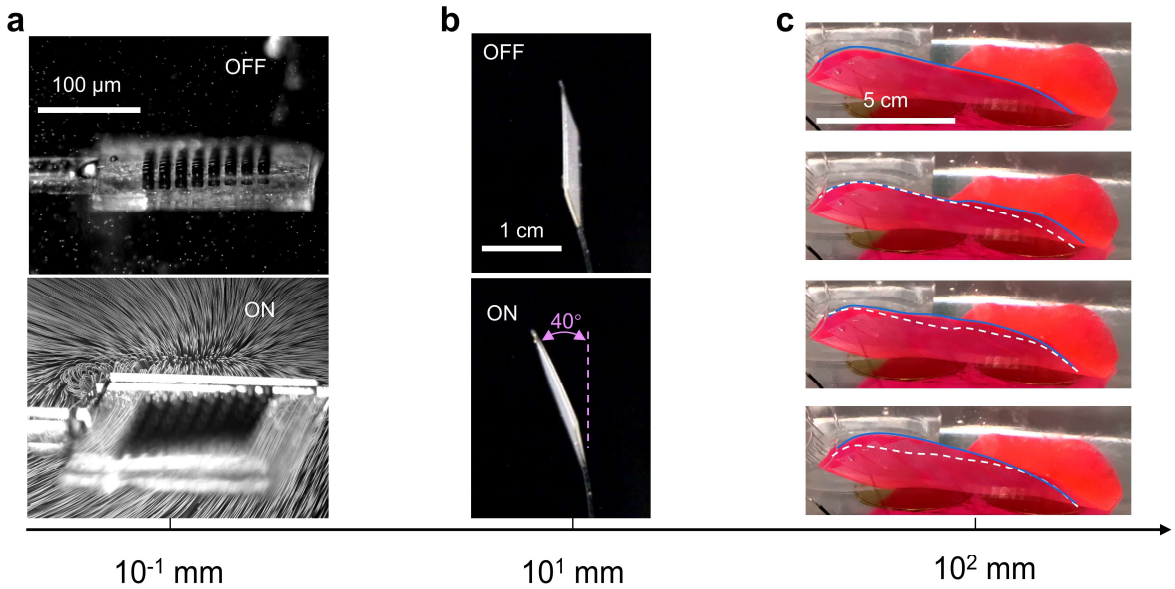


**Extended Data Fig. 9 | Artificial muscles functioning at scales from $10^{-1}$ mm to $10^{2}$ mm. a,** A microscale rotator featuring an asymmetric 8 × 8 microbubble array (12 μm × 50 μm). The upper and lower panels show the microrotator with ultrasound on and off, respectively, at 95.5 kHz and 60 $V_{PP}$. **b,** A millimeter-scale rotator with an asymmetric 400 × 200 microbubble array (12 μm × 50 μm). The upper and lower panels show the device with ultrasound on and off, respectively, under the same driving conditions. The purple dashed line indicates the original position of the artificial muscle. **c,** A macroscale stingraybot equipped with artificial muscles comprising variable-size microbubble arrays (40 μm × 150 μm, 60 μm × 150 μm, 80 μm × 150 μm, respectively), demonstrating undulatory motion under excitation (10-90 kHz, duty cycles 2 s, 120 $V_{PP}$). The blue line marks the current location of the fin edge, while the white dashed line shows its position in the previous frame of the time-lapse image.